A High-Order Implicit Bound-Preserving Discontinuous Galerkin Method for Incompressible Miscible Displacement in Porous Media

Xiaojuan Gong*
School of General Education, Yantai Institute of Science and Technology, Yantai, China
**Corresponding Author*

Abstract: A high-order implicit bound-preserving discontinuous Galerkin method is developed for incompressible miscible displacement in porous media. The pressure–velocity system and the concentration equation are discretized in discontinuous finite element spaces, and backward differentiation formulas are used for time integration. Following a predictor–corrector strategy, a standard implicit DG step first produces a provisional concentration. A space-dependent Lagrange multiplier then enforces the Karush–Kuhn–Tucker conditions associated with the interval constraint, while an additional scalar multiplier preserves the porosity-weighted mass supplied by the DG prediction. The corrector reduces to pointwise formulas and one scalar monotone equation. The nodal bound, discrete mass balance, and compatibility of the two-component concentrations are established. Numerical experiments verify third-order accuracy, elimination of nonphysical undershoots and overshoots, and mass conservation in a source-free transport problem. Two field-oriented tests further demonstrate channeling in a strongly heterogeneous five-spot pattern and contaminant removal from an aquifer containing conductive pathways and a low-permeability barrier.

Keywords: Incompressible Miscible Displacement; Discontinuous Galerkin Method; Bound Preservation; Mass Conservation; Lagrange Multiplier; Bdf Method.

1. Introduction

Miscible displacement in porous media describes the transport of one fluid by another when the two phases mix on the pore scale. It is a basic model for enhanced oil recovery, subsurface contaminant migration, groundwater remediation, and related filtration processes. At the Darcy scale, the pressure and velocity are governed by an elliptic problem, whereas the concentration satisfies a convection–diffusion equation whose coefficients depend on the velocity and, through the viscosity, on the concentration itself. The different character of these equations and their nonlinear coupling are the principal sources of difficulty in both analysis and computation.

The concentration is a volume fraction and therefore has to remain in the physical interval $[0,1]$. This constraint is not merely qualitative. Viscosity laws are commonly evaluated only on the admissible interval, and even small negative values may lead to an incorrect mobility ratio or a loss of solvability in a nonlinear iteration. In convection-dominated regimes, however, high-order polynomial approximations readily develop undershoots and overshoots near steep fronts. The difficulty is compounded by heterogeneous permeability, anisotropic dispersion, and the localized source terms used to represent injection and production wells.

Many numerical methods have been proposed for incompressible miscible displacement. Early interior-penalty and mixed finite element formulations can be found in [1–3]. Combined mixed finite element and discontinuous Galerkin approximations were subsequently studied in [4–5], and convergence for low-regularity solutions was established in [6]. Discontinuous Galerkin (DG) methods are particularly attractive for transport in heterogeneous media because they are locally conservative, accommodate discontinuous coefficients, and permit high-order approximation without enforcing interelement continuity. The local DG and interior-penalty constructions developed for diffusion and convection–diffusion problems provide the basic tools used here [7–8].

Recent developments include bound-preserving LDG schemes for porous-media two-phase flow [9], hybridized DG discretizations for Darcy flow

and transport [10], oscillation-free DG simulations of miscible viscous fingering [11], and an efficient cell-centered Galerkin method for heterogeneous miscible displacement [12].

High-order accuracy alone does not enforce a physical bound. Existing positivity- and bound-preserving strategies may be divided into several broad classes. Discrete-maximum-principle methods build the bound into the spatial operator, but their mesh and order requirements can be restrictive. Convex splitting and nonlinear reformulation techniques can provide strong structural properties at the cost of a nonlinear solve. A cutoff is inexpensive, but a plain cutoff generally changes the total mass. For explicit DG schemes, a widely used alternative is to prove that the cell average is admissible under a CFL condition and then rescale the polynomial around its average [13–16]. Such limiters preserve high order for smooth solutions, but their admissible-average argument is tied to the time discretization and becomes less convenient for large implicit steps.

The two-component identity offers another route. Writing $c_1=c$ and $c_2=1-c$, the upper bound for one component is equivalent to positivity of the other. Guo and Yang [17] used consistent numerical fluxes and positivity limiters to construct a second-order bound-preserving DG method for compressible miscible displacement. This observation is also useful in the incompressible problem, but it does not by itself resolve the interaction between high-order implicit time integration, nodal bounds, and the discrete mass balance.

Cheng and Shen [18–19] introduced a Lagrange multiplier framework that separates these issues. A standard spatial discretization and a standard implicit or implicit–explicit time step are first used to compute a provisional solution. A second, inexpensive correction enforces the Karush–Kuhn–Tucker (KKT) conditions at the collocation points. A spatially dependent multiplier activates only where the bound is attained, while a scalar multiplier restores the prescribed mass. The correction can be solved pointwise once the scalar multiplier is known. Consequently, the procedure is largely independent of the spatial discretization and can be attached to an existing solver without replacing its principal linear or nonlinear algebra.

The purpose of the present work is to combine this predictor–corrector idea with a high-order DG approximation of incompressible miscible displacement. The pressure–velocity equations and the concentration equation are discretized in a common discontinuous finite element space. Alternating fluxes are used for the Darcy variables, an upwind flux is used for convection, and an interior-penalty form is used for dispersion. The numerical fluxes are chosen consistently so that the discrete equations for c and $1-c$ retain the same algebraic structure. Time integration is based on backward differentiation formulas (BDF), and the Lagrange multiplier correction is applied after the implicit DG prediction.

Two aspects require special attention in this coupled setting. First, the continuous concentration mass is not necessarily constant in the presence of wells. The corrector must therefore preserve the mass delivered by the conservative DG predictor, rather than impose the initial mass indiscriminately. Second, the admissible interval has two active boundaries. The quadratic constraint function $g(c)=c(1-c)$ is used to obtain a three-branch pointwise formula: values inside (0,1) are unchanged apart from the global mass shift, while values outside the interval are placed on the appropriate active boundary. The remaining unknown is one scalar multiplier determined by a continuous monotone equation.

The resulting method preserves the nodal bounds $0\le c_h\le 1$ and the porosity-weighted mass of the provisional DG solution. It does not alter the pressure–velocity solver, and its additional cost consists of scalar reductions and pointwise updates. The KKT formulation also clarifies the relation between the correction and the usual cutoff procedure. When the global multiplier is omitted, the corrector reduces to cutoff. With the multiplier retained, the mass change introduced by cutoff is redistributed over the inactive set.

The numerical experiments examine complementary aspects of the method. Two manufactured solutions are used to measure the convergence rate and to compare the corrected and uncorrected DG solutions. Two controlled transport tests illustrate concentration evolution and source-free mass conservation. Finally, a heterogeneous five-spot displacement and a channelized-aquifer remediation problem test the method under permeability contrasts, localized wells, and preferential flow. The results show that the correction removes nonphysical values without changing the observed third-order convergence of the underlying scheme, while the application tests retain the discrete well balance

to near machine precision.

The paper is organized as follows. Section 2 introduces the model, its mass balance, and the DG spatial discretization. Section 3 describes the implicit BDF prediction. The Lagrange multiplier corrector, its analytical properties, and its implementation are presented together in Section 4. Section 5 contains six numerical examples, and concluding remarks are given in Section 6.

2. Model and DG Spatial Discretization

2.1 Governing Equations, Physical Constraints, and Mass Balance

Let $\Omega\subset\mathbb{R}^2$ be a bounded polygonal domain and let $T>0$. Set $Q_T=\Omega\times(0,T]$. The incompressible miscible displacement model is

$$\nabla\cdot\boldsymbol{u}=q,(\boldsymbol{x},t)\in Q_T, \tag{1}$$

$$a(c)\boldsymbol{u}+\nabla p=0,(\boldsymbol{x},t)\in Q_T, \tag{2}$$

$$\phi c_t+\nabla\cdot(\boldsymbol{u}c)-\nabla\cdot(\boldsymbol{D}(\boldsymbol{u})\nabla c)=\tilde{c}\,q,\quad(\boldsymbol{x},t)\in Q_T. \tag{3}$$

Here p is the pressure, $\boldsymbol{u}$ is the Darcy velocity, and c is the volume concentration of the injected component. The mobility coefficient is written as

$$a(c)=\frac{\mu(c)}{\kappa(\boldsymbol{x})}, \tag{4}$$

where μ and κ denote viscosity and absolute permeability. It is assumed that

$$\begin{aligned}&0<\phi_0\le\phi(\boldsymbol{x})\le\phi_1,\\&0<\kappa_0\le\kappa(\boldsymbol{x})\le\kappa_1,\\&0<\mu_0\le\mu(s)\le\mu_1\quad(0\le s\le1).\end{aligned} \tag{5}$$

The source q is positive at injection locations and negative at production locations. The prescribed concentration $\tilde{c}$ is the injected concentration on $\{q>0\}$ and is taken to be the resident concentration on $\{q<0\}$. This convention gives the usual well contribution without creating or removing the complementary component artificially.

The hydrodynamic dispersion tensor contains molecular diffusion and mechanical dispersion. For $\boldsymbol{u}\neq0$, it is written as

$$\boldsymbol{D}(\boldsymbol{u})=\phi(d_{\mathrm{mol}}\boldsymbol{I}+d_{\mathrm{long}}|\boldsymbol{u}|\boldsymbol{E}(\boldsymbol{u})+d_{\mathrm{tran}}|\boldsymbol{u}|\boldsymbol{E}^{\perp}(\boldsymbol{u})), \tag{6}$$

where

$$E_{ij}(\boldsymbol{u})=\frac{u_iu_j}{|\boldsymbol{u}|^2},\qquad \boldsymbol{E}^{\perp}(\boldsymbol{u})=\boldsymbol{I}-\boldsymbol{E}(\boldsymbol{u}). \tag{7}$$

At $\boldsymbol{u}=0$, $\boldsymbol{E}(\boldsymbol{0})=0$ is set. The coefficients satisfy $d_{\mathrm{mol}},d_{\mathrm{long}},d_{\mathrm{tran}}\ge0$, so $\boldsymbol{D}$ is symmetric positive semidefinite. Strict positivity is needed only when a coercive diffusion estimate is invoked; the formulation itself also covers vanishing molecular diffusion.

For the closed system, the following conditions are imposed:

$$\boldsymbol{u}\cdot\boldsymbol{n}=0,\qquad(\boldsymbol{D}(\boldsymbol{u})\nabla c-c\boldsymbol{u})\cdot\boldsymbol{n}=0\quad\text{on }\partial\Omega, \tag{8}$$

and prescribe $c(\boldsymbol{x},0)=c_0(\boldsymbol{x})$. Nonhomogeneous normal fluxes and periodic conditions are used in some numerical tests; their boundary terms are inserted in the standard way. Solvability of the no-flow pressure problem requires $\int_\Omega q\,\mathrm{d}\boldsymbol{x}=0$. The pressure is made unique by the normalization

$$\int_\Omega p(\boldsymbol{x},t)\,\mathrm{d}\boldsymbol{x}=0. \tag{9}$$

The admissible concentration set is

$$\mathrm{A}=\{v:0\le v(\boldsymbol{x})\le1\text{ a.e. in }\Omega\}. \tag{10}$$

For a two-component mixture, $c_1=c$ and $c_2=1-c$. Hence preservation of A is equivalent to positivity of both component concentrations and implies $c_1+c_2=1$ pointwise.

The porosity-weighted mass of the first component is

$$\mathcal{M}(c(t))=\int_\Omega\phi(\boldsymbol{x})c(\boldsymbol{x},t)\,\mathrm{d}\boldsymbol{x}. \tag{11}$$

Integrating (3) over Ω and using (8) gives

$$\frac{\mathrm{d}}{\mathrm{d}t}\mathcal{M}(c(t))=\int_\Omega\tilde{c}\,q\,\mathrm{d}\boldsymbol{x}. \tag{12}$$

Thus mass is constant when $q=0$, but it generally changes in the presence of wells. This distinction is important for the correction step: the numerical corrector must match the mass dictated by the discrete form of (12), not necessarily the initial mass.

The equation for $c_2=1-c$ follows by subtracting (3) from (1). With $\tilde{c}_2=1-\tilde{c}$, one obtains

$$\phi(c_2)_t+\nabla\cdot(\boldsymbol{u}c_2)-\nabla\cdot(\boldsymbol{D}(\boldsymbol{u})\nabla c_2)=\tilde{c}_2q. \tag{13}$$

The two transport equations therefore have the same differential structure. The DG fluxes below are chosen so that this identity also holds at the discrete level.

2.2 Mesh, Traces, and DG Formulation

The basic notation is illustrated in the two-dimensional case on a rectangular mesh. Let $x_{\frac12},\dots,x_{N_x+\frac12}$ and $y_{\frac12},\dots,y_{N_y+\frac12}$ denote the mesh points in the x- and y-directions, respectively. The computational cell is defined as $K_{ij}=I_i\times J_j$ for $i=1,\dots,N_x$ and $j=1,\dots,N_y$, where $I_i=(x_{i-\frac12},x_{i+\frac12})$ and

$J_j=(y_{j-\frac{1}{2}},y_{j+\frac{1}{2}})$. The collection $\Omega_h=\{K_{ij}\}$ forms a partition of the domain Ω. For simplicity, a generic cell is denoted by K. The mesh sizes in the two coordinate directions are $\Delta x_i=x_{i+\frac{1}{2}}-x_{i-\frac{1}{2}}$ and $\Delta y_j=y_{j+\frac{1}{2}}-y_{j-\frac{1}{2}}$. A uniform mesh is assumed throughout, i.e., $\Delta x=\Delta x_i$ and $\Delta y=\Delta y_j$. Let Γ denote the set of all cell interfaces and define $\Gamma_0=\Gamma\setminus\partial\Omega$ as the set of interior interfaces. For any interface $e\in\Gamma$, its length is denoted by $|e|$. The unit normal vector $\boldsymbol{n}_e$ is defined by $\boldsymbol{n}_e=\boldsymbol{n}_x=(1,0)^T$ if e is parallel to the y-axis and $\boldsymbol{n}_e=\boldsymbol{n}_y=(0,1)^T$ if e is parallel to the x-axis.

The finite element space is chosen as

$$W_h=\{z:z|_K\in P^k(K),\forall K\in\Omega_h\}, \tag{14}$$

where $P^k(K)$ denotes the space of polynomials of degree at most k on the element K. For any $v\in W_h$, the symbols $v^+_{i-\frac{1}{2},j}$, $v^-_{i+\frac{1}{2},j}$, $v^+_{i,j-\frac{1}{2}}$, and $v^-_{i,j+\frac{1}{2}}$ denote the traces of v on the left, right, bottom, and top edges of the cell K_{ij}, respectively. The jump and average of v across each cell interface are defined as

$$[v]=v^+-v^-,\quad \{v\}=\frac{1}{2}(v^++v^-). \tag{15}$$

For simplicity, the same symbols p, c, and $\boldsymbol{u}$ are also used for their numerical approximations. The DG scheme aims to find $p,c\in W_h$ and $\boldsymbol{u}\in\boldsymbol{W}_h=W_h\times W_h$ such that, for any test functions $\xi,\zeta\in W_h$ and $\boldsymbol{\eta}\in\boldsymbol{W}_h$, the following variational formulations hold:

$$-(q,\xi)=(\boldsymbol{u},\nabla\xi)+\sum_{e\in\Gamma_0}\int_e \hat{\boldsymbol{u}}\,[\xi]\cdot\boldsymbol{n}_e ds, \tag{16}$$

$$(a(c)\boldsymbol{u},\boldsymbol{\eta})=(p,\nabla\cdot\boldsymbol{\eta})+\sum_{e\in\Gamma}\int_e \hat{p}\,[\boldsymbol{\eta}\cdot\boldsymbol{n}_e]ds, \tag{17}$$

$$\begin{aligned}&(\phi c_t,\zeta)=(\boldsymbol{u}c-\boldsymbol{D}(\boldsymbol{u})\nabla c,\nabla\zeta)\\&+(\tilde{c}q,\zeta)\\&+\sum_{e\in\Gamma_0}\int_e \widehat{\boldsymbol{u}c}\cdot\boldsymbol{n}_e[\zeta]ds\\&-\sum_{e\in\Gamma_0}\int_e\begin{pmatrix}\{\boldsymbol{D}(\boldsymbol{u})\nabla c\cdot\boldsymbol{n}_e\}[\zeta]\\+\{\boldsymbol{D}(\boldsymbol{u})\nabla\zeta\cdot\boldsymbol{n}_e\}[c]\\+\dfrac{\tilde{\alpha}}{|e|}[c][\zeta]\end{pmatrix}ds,\end{aligned} \tag{18}$$

where $(u,v)=\int_\Omega uv\,dxdy$. In (16)-(18), $\hat{p}$, $\hat{\boldsymbol{u}}$, and $\widehat{\boldsymbol{u}c}$ denote the numerical fluxes. For the diffusion term, the following definitions are adopted:

$$\hat{\boldsymbol{u}}|_e=\boldsymbol{u}^+|_e,\quad \hat{p}|_e=p^-|_e, \tag{19}$$

For the convective flux, the scheme adopts the formulation

$$\widehat{\boldsymbol{u}c}\cdot\boldsymbol{n}_e=(\boldsymbol{u}^+\cdot\boldsymbol{n}_e)c^+-\alpha_e[c]. \tag{20}$$

Here α_e is a nonnegative face parameter and $\tilde{\alpha}>0$ is the interior-penalty parameter. Formula (20) defines the scalar normal flux used in (18); it is therefore dimensionally consistent with the face integral.

To derive the equation for c_2, the following definition from [17] is recalled:

Definition 2.1. The concentration flux is said to be consistent with the velocity flux if $\widehat{\boldsymbol{u}c}\cdot\boldsymbol{n}_e=\hat{\boldsymbol{u}}\cdot\boldsymbol{n}_e$ when $c=1$ in Ω.

Clearly, the numerical flux in (20) is consistent with the velocity flux in (19), which implies that $(\widehat{\boldsymbol{u}c}+\widehat{\boldsymbol{u}c_2})\cdot\boldsymbol{n}_e=\hat{\boldsymbol{u}}\cdot\boldsymbol{n}_e$, where $c_2=1-c$. Then by choosing $\xi=\zeta$ in (16) and subtracting (18) from it, the following equation for c_2 is obtained:

$$\begin{aligned}&(\phi c_{2t},\zeta)=(\boldsymbol{u}c_2-\boldsymbol{D}(\boldsymbol{u})\nabla c_2,\nabla\zeta)\\&+(\tilde{c}_2q,\zeta)+\sum_{e\in\Gamma_0}\int_e \widehat{\boldsymbol{u}c_2}\cdot\boldsymbol{n}_e[\zeta]ds\\&-\sum_{e\in\Gamma_0}\int_e\begin{pmatrix}\{\boldsymbol{D}(\boldsymbol{u})\nabla c_2\cdot\boldsymbol{n}_e\}[\zeta]\\+\{\boldsymbol{D}(\boldsymbol{u})\nabla\zeta\cdot\boldsymbol{n}_e\}[c_2]\\+\dfrac{\tilde{\alpha}}{|e|}[c_2][\zeta]\end{pmatrix}ds,\end{aligned} \tag{21}$$

where $\tilde{c}_2=1-\tilde{c}$. It is easy to check that (21) is exactly (18) with c replaced by c_2.

2.3 Conservation, Component Compatibility, and the Darcy Estimate

The preceding construction retains two structural identities of the continuous problem. The first is local conservation. Let χ_K be one on a fixed element K and zero on all other elements. Since $\chi_K\in W_h$, taking $\zeta=\chi_K$ in (18) yields an elementwise balance in which the only coupling to neighboring elements is through single-valued numerical fluxes on ∂K. Contributions on a common face occur with opposite signs for the two adjacent elements. Summation over all elements therefore cancels every interior flux.

The second identity is the global mass balance. Taking $\zeta=1$ in (18) makes all volume-gradient, jump, and penalty terms vanish and gives

$$\frac{\mathrm{d}}{\mathrm{d}t}(\phi c_h,1)=(\tilde{c}q,1). \tag{22}$$

In particular, $(\phi c_h,1)$ is constant for a source-free problem with closed or periodic boundaries. This simple identity is the mass target used by the Lagrange multiplier corrector.

Proposition 2.1 (Compatibility of the component equations). Assume that the concentration flux is consistent with the velocity flux in the sense of Definition 2.1. If $c_{1,h}+c_{2,h}=1$ initially, then the semidiscrete equations for $c_{1,h}$ and $c_{2,h}$ obtained from (18) satisfy the same algebraic relation as (3)–(13).

Proof. Since $[c_{1,h}]+[c_{2,h}]=0$ and $c^{+}_{1,h}+c^{+}_{2,h}=1$, the numerical convective fluxes satisfy $(\widehat{\boldsymbol{u}c}_1+\widehat{\boldsymbol{u}c}_2)\cdot \boldsymbol{n}_e=\hat{\boldsymbol{u}}\cdot \boldsymbol{n}_e$. The diffusion terms cancel because $\nabla(c_{1,h}+c_{2,h})=0$, and the source terms add to q. Adding the two transport equations therefore recovers the discrete divergence equation. Subtracting either component equation from that identity gives the other. □

The positive penalty parameter $\tilde{\alpha}$ is chosen sufficiently large for the symmetric interior-penalty diffusion form to be coercive when $\boldsymbol{D}$ is uniformly positive definite. The face parameter α_e is taken no smaller than one half of the largest normal advective speed on that face. These choices control interelement oscillations, but they do not imply the nodal bound $0\le c_h\le 1$; that property is enforced by the corrector introduced in Section 4.

The pressure equation has a one-dimensional null space under the no-flow condition, so the discrete pressure space is restricted by $(p_h,1)=0$. The compatibility condition $(q,1)=0$ follows by taking the constant test function in the discrete divergence equation. On this mean-zero subspace, the Darcy bilinear form controls the velocity. Indeed, the alternating fluxes in (16)–(17) are selected so that their interior-face contributions cancel when $\xi=p_h$ and $\boldsymbol{\eta}=\boldsymbol{u}_h$. Consequently, for homogeneous normal fluxes,

$$(a(c_h)\boldsymbol{u}_h,\boldsymbol{u}_h)=(q,p_h). \tag{23}$$

Using (5), the Cauchy–Schwarz inequality, and the discrete inf–sup estimate for the pressure–velocity pair gives, formally,

$$\|\boldsymbol{u}_h\|_{0,\Omega}\le C\|q\|_{0,\Omega}, \tag{24}$$

where C depends on the mobility bounds and mesh regularity but not on the time step. Relation (23) is also useful in the nonlinear iteration: loss of this balance is an indication that the pressure normalization or a boundary numerical flux has been assembled inconsistently.

3. Implicit Time Discretization

3.1 BDF Formulas and DG Residual Operators

Let $t^n=n\Delta t$ and let v^n denote an approximation to $v(t^n)$. The k-step backward differentiation formula and an order-$(k-1)$ extrapolation are used for the time derivative and previously computed multiplier terms, respectively. Following [18–19], define α_k, A_k, and B_{k-1} by

$$\begin{aligned} &k=1:\quad \alpha_1=1, A_1(v^n)=v^n,\\ &B_0(v^n)=0, \end{aligned} \tag{25}$$

$$\begin{aligned} &k=2:\quad \alpha_2=\frac{3}{2},\\ &A_2(v^n)=2v^n-\frac{1}{2}v^{n-1},\\ &B_1(v^n)=v^n, \end{aligned} \tag{26}$$

$$\begin{aligned} &k=3:\quad \alpha_3=\frac{11}{6},\\ &A_3(v^n)=3v^n-\frac{3}{2}v^{n-1}+\frac{1}{3}v^{n-2},\\ &B_2(v^n)=2v^n-v^{n-1}. \end{aligned} \tag{27}$$

Thus $(\alpha_k v^{n+1}-A_k(v^n))/\Delta t$ is a k th-order approximation to $v_t(t^{n+1})$. The operator B_{k-1} is not needed for the physical terms treated implicitly; it appears in the predictor–corrector splitting so that the multiplier contribution is represented at the same order.

It is convenient to collect the spatial forms from Section 2. For $\xi,\zeta\in W_h$ and $\boldsymbol{\eta}\in \boldsymbol{W}_h$, set

$$\mathscr{B}_u(\boldsymbol{u};\zeta)=(\boldsymbol{u},\nabla\zeta)+\sum_{e\in\Gamma_0}\int_e \hat{\boldsymbol{u}}\cdot \boldsymbol{n}_e[\zeta]\,\mathrm{d}s, \tag{28}$$

$$\begin{aligned} &\mathscr{B}_p(p,\boldsymbol{u},c;\boldsymbol{\eta})\\ &=(p,\nabla\cdot\boldsymbol{\eta})+\sum_{e\in\Gamma}\int_e \hat{p}\,[\boldsymbol{\eta}\cdot\boldsymbol{n}_e]\,\mathrm{d}s\\ &-(a(c)\boldsymbol{u},\boldsymbol{\eta}), \end{aligned} \tag{29}$$

$$\begin{aligned} &\mathrm{C}_h(\boldsymbol{u},c;\zeta)=(\boldsymbol{u}c-\boldsymbol{D}(\boldsymbol{u})\nabla c,\nabla\zeta)\\ &+\sum_{e\in\Gamma_0}\int_e \widehat{\boldsymbol{u}c}\cdot\boldsymbol{n}_e[\zeta]\,\mathrm{d}s\\ &-\sum_{e\in\Gamma_0}\int_e (\{\boldsymbol{D}(\boldsymbol{u})\nabla c\cdot\boldsymbol{n}_e\}[\zeta]\\ &+\{\boldsymbol{D}(\boldsymbol{u})\nabla\zeta\cdot\boldsymbol{n}_e\}[c]\\ &+\frac{\tilde{\alpha}}{|e|}[c][\zeta])\,\mathrm{d}s. \end{aligned} \tag{30}$$

The pressure–velocity equations are $\mathscr{B}_u(\boldsymbol{u};\zeta)=-(q,\zeta)$ and $\mathscr{B}_p(p,\boldsymbol{u},c;\boldsymbol{\eta})=0$. The semidiscrete concentration equation is

$$(\phi c_t,\zeta)=\mathrm{C}_h(\boldsymbol{u},c;\zeta)+(\tilde{c}q,\zeta). \tag{31}$$

3.2 Implicit Prediction, Target Mass, and Initialization

Assume that c_h^j, the nodal multiplier λ_h^j, and the scalar multiplier ξ_h^j are known for the required previous levels. The provisional solution $(p_h^{n+1},\boldsymbol{u}_h^{n+1},\tilde{c}_h^{n+1})$ is defined by

$$\mathscr{B}_u\big(\boldsymbol{u}_h^{n+1};\xi\big)=-\big(q^{n+1},\xi\big), \tag{32}$$

$$\mathscr{B}_p\big(p_h^{n+1},\boldsymbol{u}_h^{n+1},\tilde{c}_h^{n+1};\boldsymbol{\eta}\big)=0, \tag{33}$$

$$\begin{aligned}&(\phi\frac{\alpha_k\tilde{c}_h^{n+1}-A_k(c_h^n)}{\Delta t},\zeta)\\&=\mathrm{C}_h(\boldsymbol{u}_h^{n+1},\tilde{c}_h^{n+1};\zeta)\\&\quad+(\tilde{c}^{\,n+1}q^{n+1},\zeta)\\&\quad+(B_{k-1}(\lambda_h^n g'(c_h^n)+\xi_h^n),\zeta)_h,\end{aligned} \tag{34}$$

These equations hold for every $\xi,\zeta\in W_h$ and $\boldsymbol{\eta}\in\boldsymbol{W}_h$. Here and below $\tilde{c}$ with no subscript denotes the concentration carried by the well source, while $\tilde{c}_h^{n+1}$ denotes the provisional DG solution; the distinction is clear from the context. The constraint function g is defined in Section 4.

Equations (32)–(34) may be solved monolithically. In the implementation used for the numerical tests, the concentration dependence of the viscosity is handled by a fixed-point iteration: given a concentration iterate, solve the Darcy equations, assemble the dispersion tensor, solve the implicit concentration equation, and repeat until the relative change of the concentration is below the prescribed nonlinear tolerance. The bound correction is performed only after the coupled prediction has converged. This order is important because clipping intermediate nonlinear iterates would change the equations being solved.

For a constant viscosity the Darcy problem is independent of concentration and is solved once per time level. When $\mu=\mu(c)$, the pressure normalization is imposed at every fixed-point iteration. The matrices associated with the mass, penalty, and derivative terms have the same sparsity pattern at all time levels; only coefficient-weighted entries need to be updated.

Let $M_h^n=(\phi c_h^n,1)_h$. The mass to be imposed after the corrector is the BDF discretization of (12):

$$\begin{aligned}M_{\mathrm{tar}}^{n+1}=&\frac{1}{\alpha_k}\\&(A_k(M_h^n)+\Delta t\,(\tilde{c}^{\,n+1}q^{n+1},1)_h).\end{aligned} \tag{35}$$

For $q=0$, this formula is the BDF form of constant mass. For $k=1$ it reduces to $M_{\mathrm{tar}}^{n+1}=M_h^n$; for higher-order formulas it preserves the corresponding multistep invariant. Using (35), rather than simply copying the provisional mass, ensures that the correction remains consistent with the physical source balance even when multiplier history terms occur in (34).

The first two levels required by BDF3 are computed successively with BDF1 and BDF2. In a manufactured-solution convergence test, exact history values may be used instead so that the temporal order of the interior BDF3 steps is measured without a starting error. In either case the correction is applied at every starting level, and the multiplier histories that do not yet exist are set to zero. All numerical experiments below use BDF3 after initialization.

4. Bound-Preserving Correction with Lagrange Multipliers

The implicit prediction (32)–(34) is conservative, but its nodal values need not be contained in [0,1]. A correction is now derived that enforces the interval constraint and the target mass (35). The construction follows the predictor–corrector Lagrange multiplier framework of [18–19], specialized to the concentration variable and the porosity-weighted mass of miscible displacement.

4.1. Nodal KKT System and Pointwise Correction

Let Σ_h be the set of interpolation or collocation points on which the bound is imposed. Points carrying an essential Dirichlet condition are excluded, whereas points on a Neumann or periodic boundary are included. Let

$$\begin{aligned}(v,w)_h=&\sum_{z\in\Sigma_h}\omega_z\,v(z)w(z),\\&\omega_z>0,\end{aligned} \tag{36}$$

be the quadrature inner product. For a DG finite element space, the sum is understood element by element; a point shared geometrically by two elements has two traces and therefore two DG degrees of freedom.

The interval constraint is represented by

$$\begin{aligned}g(c)=&c(1-c),\\g'(c)=&1-2c.\end{aligned} \tag{37}$$

The condition $g(c)\ge 0$ is equivalent to $0\le c\le 1$. Introducing a space-dependent multiplier $\lambda_h(z,t)$ gives the expanded nodal system

$$\phi c_t-\mathscr{L}_h(c,\boldsymbol{u})=\lambda_h g'(c),z\in\Sigma_h, \tag{38}$$

$$\begin{aligned}\lambda_h\ge 0,\quad g(c)\ge 0,\\\lambda_h g(c)=0,z\in\Sigma_h.\end{aligned} \tag{39}$$

Here $\mathscr{L}_h$ denotes the DG transport operator including the well source. The second line consists of the KKT conditions. If $0<c<1$, then

$\lambda_h=0$ and the original DG equation is recovered. At $c=0$ or $c=1$, the multiplier acts in the direction $g'(0)=1$ or $g'(1)=-1$, respectively, and prevents the solution from leaving the admissible interval.

The multiplier in (38) is local and does not by itself preserve mass. A correction at the lower boundary adds concentration, whereas a correction at the upper boundary removes it. A second multiplier $\xi_h(t)$ that is independent of the spatial variable is therefore introduced. Its role is to redistribute the net mass change generated by the active nodal multipliers.

For the higher-order corrector, define the extrapolated multiplier contribution

$$H_h^n(z)= B_{k-1}(\lambda_h^n(z)g'(c_h^n(z))+\xi_h^n). \tag{40}$$

After the prediction step has produced $\tilde{c}_h^{n+1}$, the corrected concentration, the nodal multiplier, and the scalar multiplier satisfy

$$\frac{\alpha_k\phi(z)}{\Delta t}(c_h^{n+1}(z)-\tilde{c}_h^{n+1}(z)) =\lambda_h^{n+1}(z)g'(c_h^{n+1}(z))+\xi_h^{n+1} -H_h^n(z), \tag{41}$$

$$\lambda_h^{n+1}(z)\geq 0, \qquad g\left(c_h^{n+1}(z)\right)\geq 0, \qquad \lambda_h^{n+1}(z)g(c_h^{n+1}(z))=0, \tag{42}$$

$$(\phi c_h^{n+1},1)_h=M_{\text{tar}}^{n+1}. \tag{43}$$

The history term in (41) is the counterpart of the final term in (34). Adding the prediction and correction equations leaves the current multiplier contribution, while the mass equation determines its spatial mean. If all history terms are omitted, the formula reduces to the high-order cutoff variant discussed in [19].

Assume temporarily that ξ_h^{n+1} is known and define

$$r_z(\xi)=\tilde{c}_h^{n+1}(z) +\frac{\Delta t}{\alpha_k\phi(z)}(\xi-H_h^n(z)). \tag{44}$$

Equations (41)–(42) can then be solved independently at each $z\in\Sigma_h$. The result is written more compactly by setting $r=r_z(\xi_h^{n+1})$:

$$c_h^{n+1}(z)=\begin{cases}0, & r\leq 0,\\ r, & 0<r<1,\\ 1, & r\geq 1,\end{cases}$$

$$\lambda_h^{n+1}(z)=\begin{cases}-\dfrac{\alpha_k\phi(z)}{\Delta t}r, & r\leq 0,\\ 0, & 0<r<1,\\ \dfrac{\alpha_k\phi(z)}{\Delta t}(r-1), & r\geq 1.\end{cases} \tag{45}$$

Equivalently,

$$c_h^{n+1}(z)=\text{clip}(r_z(\xi_h^{n+1}),0,1), \quad \text{clip}(s,0,1) =\min\{1,\max\{0,s\}\}. \tag{46}$$

The KKT formulation is therefore not an additional constrained nonlinear solve: the nodal part of the corrector is explicit.

4.2. Scalar Mass Equation

It remains to determine ξ_h^{n+1}. For any scalar ξ, introduce the active sets

$$\Sigma_h^-(\xi)=\{z\in\Sigma_h: r_z(\xi)\leq 0\}, \tag{47}$$

$$\Sigma_h^0(\xi)=\{z\in\Sigma_h: 0<r_z(\xi)<1\}, \tag{48}$$

$$\Sigma_h^+(\xi)=\{z\in\Sigma_h: r_z(\xi)\geq 1\}. \tag{49}$$

Substitution of (45) into (43) gives the scalar equation

$$F^{n+1}(\xi)=\sum_{z\in\Sigma_h^0(\xi)}\omega_z\,\phi(z)r_z(\xi)+\sum_{z\in\Sigma_h^+(\xi)}\omega_z\,\phi(z)-M_{\text{tar}}^{n+1}=0. \tag{50}$$

No contribution is made by $\Sigma_h^-(\xi)$. The function F^{n+1} is continuous, piecewise affine, and nondecreasing. Its derivative can change when an active set changes, so a plain Newton iteration is not attractive. A secant method, as used in [18–19], requires only evaluations of the discrete mass:

$$\xi^{(m+1)}=\xi^{(m)}-\frac{F^{n+1}(\xi^{(m)})(\xi^{(m)}-\xi^{(m-1)})}{F^{n+1}(\xi^{(m)})-F^{n+1}(\xi^{(m-1)})}. \tag{51}$$

In practice, the secant update is safeguarded by the bracket

$$\xi_L=\min_{z\in\Sigma_h}(H_h^n(z)-\frac{\alpha_k\phi(z)}{\Delta t}\tilde{c}_h^{n+1}(z)), \tag{52}$$

$$\xi_R=\max_{z\in\Sigma_h}(H_h^n(z)+\frac{\alpha_k\phi(z)}{\Delta t}(1-\tilde{c}_h^{n+1}(z))). \tag{53}$$

At ξ_L all corrected values can be placed at the lower bound, whereas at ξ_R all can be placed at the upper bound. If a secant update leaves this interval or its denominator is too small, one bisection step is taken instead.

Interpretation of the Multipliers.

The two multipliers play distinct roles. The nodal multiplier is supported on the active set and records where the provisional DG solution attempts to cross a physical boundary. From (45),

$$\lambda_h^{n+1}(z)=0 \quad \text{on } \Sigma_h^0, \tag{54}$$

whereas it is proportional to the distance of the shifted predictor from the nearest admissible endpoint on $\Sigma_h^-\cup\Sigma_h^+$. The sign of its contribution to (41) changes between the two endpoints because $g'(0)=1$ and $g'(1)=-1$.

The scalar multiplier has no local sign restriction. Multiplying (41) by ω_z, summing over Σ_h, and using the mass constraint gives

$$\xi_h^{n+1}(1,1)_h=\frac{\alpha_k}{\Delta t}(M_{\text{tar}}^{n+1}-(\phi\tilde{c}_h^{n+1},1)_h)+(H_h^n,1) -(\lambda_h^{n+1}g'(c_h^{n+1}),1)_h. \tag{55}$$

Thus ξ_h^{n+1} balances the mass discrepancy of the prediction, the extrapolated history, and the net

contribution of the active nodes. In a positivity-only problem the active contribution has one sign; for a two-sided bound, lower and upper active nodes may partially cancel. This explains why a sign assumption on ξ_h^{n+1} is neither needed nor generally valid here.

Remark 4.1. For a source-free problem, the target mass belongs to the feasible interval provided that the initial concentration is admissible. In the presence of wells, the condition $0\le M_{\mathrm{tar}}^{n+1}\le(\phi,1)_h$ is the discrete counterpart of physical compatibility. If it fails, no function bounded by zero and one can have the requested mass, and the time step or source discretization must be reconsidered.

Relation to Positivity Correction.

The positivity-preserving method of [18] is recovered by taking $g(c)=c$ and removing the upper branch in (45). The present quadratic function (37) handles both boundaries in a single correction. Alternatively, one may apply positivity corrections to $c_1=c$ and $c_2=1-c$ separately. Flux consistency then guarantees that both component equations have the same form. The direct bound formulation is used here because it maintains $c_1+c_2=1$ by construction and requires only one scalar mass equation per time level.

4.3. Analytical Properties

Proposition 4.1. Assume $\omega_z>0$, $\phi(z)>0$, and $0\le M_{\mathrm{tar}}^{n+1}\le(\phi,1)_h$. Then the scalar equation (50) has a solution. Every solution produces a corrected concentration satisfying

$$0\le c_h^{n+1}(z)\le 1 \quad (z\in\Sigma_h),\qquad (\phi c_h^{n+1},1)_h=M_{\mathrm{tar}}^{n+1}. \tag{56}$$

If the inactive set is nonempty, the corrected concentration is unique.

Proof. The map $r_z(\xi)$ is strictly increasing and continuous for every z. Clipping preserves continuity and monotonicity, so F^{n+1} has the same properties. By (52)–(53),

$$F^{n+1}(\xi_L)=-M_{\mathrm{tar}}^{n+1}\le 0,\qquad F^{n+1}(\xi_R)=(\phi,1)_h-M_{\mathrm{tar}}^{n+1}\ge 0. \tag{57}$$

The intermediate value theorem gives a root. Formula (46) gives the bound, and (50) gives the mass identity. On an interval where the inactive set is nonempty, F^{n+1} is strictly increasing; the root and hence the corrected nodal vector are unique. If all values are active, different multipliers may represent the same corrected vector at an endpoint. □

Combining Proposition 4.1 with (35) yields the fully discrete balance

$$\alpha_k(\phi c_h^{n+1},1)_h-A_k((\phi c_h^n,1)_h)=\Delta t\,(\tilde{c}^{\,n+1}q^{n+1},1)_h. \tag{58}$$

Thus the corrector does not replace conservation by an artificial constant-mass condition. It enforces the same well balance as the DG–BDF discretization.

Two-component Identity.

Define $c_{1,h}^{n+1}=c_h^{n+1}$ and $c_{2,h}^{n+1}=1-c_h^{n+1}$. Proposition 4.1 immediately gives

$$c_{1,h}^{n+1}\ge 0,\qquad c_{2,h}^{n+1}\ge 0,\qquad c_{1,h}^{n+1}+c_{2,h}^{n+1}=1 \quad \text{on } \Sigma_h. \tag{59}$$

Together with Proposition 2.1, this shows that the algebraic component constraint is preserved by both the DG prediction and the bound correction. The component masses satisfy

$$(\phi c_{1,h}^{n+1},1)_h+(\phi c_{2,h}^{n+1},1)_h=(\phi,1)_h. \tag{60}$$

A Discrete Boundedness Estimate.

The pointwise interval constraint immediately provides an L^2-type stability bound that is independent of the time step and of the magnitude of the provisional overshoot.

Proposition 4.2. Let c_h^{n+1} be the corrected concentration. Then

$$/\!/ c_h^{n+1} /\!/_{\phi,h}^2 := (\phi c_h^{n+1},c_h^{n+1})_h\le M_{\mathrm{tar}}^{n+1}, \tag{61}$$

$$/\!/ 1-c_h^{n+1} /\!/_{\phi,h}^2\le(\phi,1)_h-M_{\mathrm{tar}}^{n+1}. \tag{62}$$

In particular, $/\!/ c_h^{n+1} /\!/_{l^\infty(\Sigma_h)}\le 1$.

Proof. For $0\le s\le 1$, $s^2\le s$ and $(1-s)^2\le 1-s$. Apply these inequalities at every $z\in\Sigma_h$, multiply by the positive weight $\omega_z\phi(z)$, and sum. Equations (43) and the component mass identity give (61)–(62). The maximum-norm bound follows directly from (46). □

Consistency of the Corrector.

For a fixed scalar shift, clipping is nonexpansive:

$$|\mathrm{clip}(r,0,1)-\mathrm{clip}(s,0,1)|\le|r-s|. \tag{63}$$

Consequently, the correction cannot amplify a pointwise perturbation in the shifted provisional solution. If the exact concentration remains a positive distance from both bounds and the provisional solution is sufficiently accurate, the active set is empty. In that case $\lambda_h^{n+1}=0$, the scalar multiplier only enforces the already consistent mass equation, and the corrected and provisional solutions coincide up to the scalar-solver tolerance.

When the exact solution reaches a bound, the multiplier need not vanish locally. The general analysis in [19] shows why the history term in (40)

is useful for retaining high-order temporal consistency. A complete error estimate for the coupled nonlinear Darcy–transport system would also require approximation estimates for the concentration-dependent velocity and is beyond the scope of the present paper. The numerical results in Section 5 show that the observed third-order convergence is unchanged by the corrector.

4.4. Algorithm and Computational Cost

At each time level, the method is implemented as follows.

1. Assemble and solve (32)–(34) for p_h^{n+1}, $\boldsymbol{u}_h^{n+1}$, and $\tilde{c}_h^{n+1}$. Iterate the concentration-dependent coefficients until the coupled nonlinear tolerance is met.
2. Compute the target mass M_{tar}^{n+1} from (35) and the extrapolated multiplier history H_h^n from (40).
3. Form the bracket (52)–(53) and solve $F^{n+1}(\xi)=0$ by the safeguarded secant iteration (51).
4. Update $(c_h^{n+1},\lambda_h^{n+1})$ pointwise using (45), and store ξ_h^{n+1} for the next BDF step.

Each evaluation of F^{n+1} requires one pass over Σ_h and one scalar reduction. The storage consists of the nodal multiplier histories required by B_{k-1} and a few scalar values. No global matrix is assembled in the correction stage, and the active-set update is completely local. The stopping criterion used in the computations is

$$\frac{|F^{n+1}(\xi^{(m)})|}{\max\{1,|M_{\mathrm{tar}}^{n+1}|\}}\le\varepsilon_{\mathrm{mass}}. \qquad (64)$$

The nonlinear prediction tolerance is chosen tighter than the discretization error, and $\varepsilon_{\mathrm{mass}}$ is chosen close to machine precision. This prevents solver errors from obscuring the conservation and convergence results.

5. Numerical Experiments

Six numerical examples are presented. Unless stated otherwise, the DG space consists of piecewise quadratic polynomials and BDF3 is used in time. Exact history values initialize BDF3 in the manufactured-solution tests; BDF1 and BDF2 are used for the first two steps of the evolution tests. All volume and face integrals are evaluated by Gaussian quadrature of sufficient degree. The nonlinear prediction iteration is stopped when the relative concentration change is below 10^{-12}, and the scalar equation (50) is solved until the relative mass residual is below 2×10^{-14}. The error is measured in the quadrature-based L^2 norm, and the minimum and maximum are taken over the nodal set Σ_h.

5.1. Manufactured-Solution Accuracy Tests

Example 5.1 (One-dimensional manufactured solution). The domain is $\Omega=(0,2\pi)$ and boundary data are induced by the exact solution. The initial condition is prescribed as

$$c(x,0)=\frac{1}{2}(1-\cos(x)).$$

For this verification problem, the divergence source and the transport forcing term are

$$q(x,t)=e^{-t}\cos x,$$
$$f(x,t)=\frac{1}{2}e^{-t}(\cos x-e^{-\gamma t}\cos(2x)),$$

where f replaces $\tilde{c}q$ on the right-hand side of (3). The remaining parameters are chosen as

$$\phi(x)=1,\qquad D(u)=\gamma,$$
$$\kappa(x)=\mu(c)=1.$$

The corresponding exact pressure, velocity, and concentration are

$$p(x,t)=e^{-t}\cos x,$$
$$u(x,t)=e^{-t}\sin x,$$
$$c(x,t)=\frac{1}{2}(1-e^{-\gamma t}\cos x),$$

where $\gamma=10^{-5}$.

For the numerical tests, the time step is taken as $\Delta t=\Delta x$ and the final time is $T=1$. The L^2 errors between the numerical and exact solutions of c are listed in Table 1. The results clearly show that the DG discretization attains third-order convergence regardless of whether the BP correction is applied, demonstrating that the proposed bound-preserving procedure does not affect the accuracy of the underlying scheme. In addition, the data in Table 1 indicate that the numerical solution obtained without the BP treatment produces values outside the physically admissible range. After incorporating the BP correction, these violations disappear and the computed concentration remains strictly within the prescribed bounds.

Table 1. Example 5.1: Accuracy Test of the DG Scheme with and Without the BP Correction.

Without BP				
N	**L² error**	**Order**	**Min(c)**	**Max(c)**
10	1.657e−03	—	−1.56e−05	1.000076
20	2.200e−04	2.91	−4.03e−05	1.000092
40	2.800e−05	2.97	−1.01e−05	1.000025
80	3.460e−06	3.02	−2.47e−06	1.000012
160	4.370e−07	2.98	−5.77e−06	1.000004
320	5.330e−08	3.04	−1.03e−06	1.000005

With BP				
N	L^2 error	Order	Min(c)	Max(c)
10	1.632e−03	—	0	1
20	2.200e−04	2.89	0	1
40	2.800e−05	2.97	0	1
80	3.460e−06	3.02	0	1
160	4.370e−07	2.98	0	1
320	5.330e−08	3.04	0	1

Example 5.2 (Two-dimensional manufactured solution). The domain is $\Omega=(0,2\pi)^2$ and boundary data are induced by the exact solution. The initial condition is prescribed as

$$c(x,y,0)=\frac{1}{2}(1-\cos(x)\cos(y)).$$

The divergence source and transport forcing are

$$q(x,y,t)=2e^{-2t}\cos x\cos y,$$

$$f(x,y,t)=e^{-2t}\begin{pmatrix}\cos(x)\cos(y)\\ +\frac{1}{2}e^{-2\gamma t}\begin{pmatrix}\cos^2(x)+\cos^2(y)\\ -4\cos^2(x)\cos^2(y)\end{pmatrix}\end{pmatrix}.$$

As in Example 5.1, f replaces $\tilde{c}q$ for the manufactured test.

The remaining parameters are given by

$$\phi(x,y)=\mu(c)=\kappa(x,y)=1,$$

$$\boldsymbol{D}(\boldsymbol{u})=\begin{pmatrix}\gamma & 0\\ 0 & \gamma\end{pmatrix}.$$

The exact fields are

$$p(x,y,t)=e^{-2t}\cos x\cos y,$$

$$\boldsymbol{u}(x,y,t)=e^{-2t}(\sin x\cos y,\cos x\sin y)^T,$$

$$c(x,y,t)=\frac{1}{2}(1-e^{-2\gamma t}\cos x\cos y),$$

where $\gamma=10^{-5}$.

In the numerical simulation, the time step is chosen as $\Delta t=\Delta x$ and the final time is $T=0.1$. The L^2 error between the numerical and exact solutions of c is reported in Table 2.

The results in Table 2 show that the DG scheme attains third-order convergence both with and without the BP correction, indicating that the proposed bound-preserving procedure does not affect the accuracy of the underlying discretization. However, in the absence of the BP treatment, the numerical concentration violates the physical bounds, producing values both below zero and above one. After applying the BP correction, these violations are completely removed, and the computed solution remains within the admissible interval. This confirms that the proposed method successfully enforces the physical bounds while retaining the high-order accuracy of the DG scheme.

Table 2. Example 5.2: Accuracy Test of the DG Scheme with and Without the BP Correction.

Without BP				
N	L^2 error	Order	Min(c)	Max(c)
10	6.706e−03	—	−3.25e−03	1.0029644
20	8.908e−04	2.91	−1.84e−04	1.0001758
40	1.179e−04	2.92	−5.32e−08	0.9999998
80	1.497e−05	2.98	3.58e−06	0.9999964
160	1.863e−06	3.01	1.83e−06	0.9999982
With BP				
N	L^2 error	Order	Min(c)	Max(c)
10	6.682e−03	—	0	1
20	8.905e−04	2.91	0	1
40	1.179e−04	2.92	0	0.9999998
80	1.497e−05	2.98	3.58e−06	0.9999964
160	1.863e−06	3.01	1.83e−06	0.9999982

5.2. Production-Driven Displacement

The next test contains no manufactured exact solution. Its purpose is to examine the interaction of a nonuniform velocity, a sink term, diffusion, and the bound correction. In contrast to the preceding tables, the relevant observations are the direction of transport, the decay caused by production, and the absence of nonphysical concentrations during the evolution.

Example 5.3 (Production-driven transport). This example is designed to examine the performance of the proposed scheme for an incompressible flow-driven miscible displacement problem. A production well acting over the entire computational domain $\Omega=[0,1]\times[0,1]$ is considered, with the sink term specified as

$$q=-2\pi^2\sin(\pi x)\sin(\pi y).$$

The initial concentration and velocity field are prescribed by

$$c(x,y,0)=\sin(\pi x)\sin(\pi y),$$

$$\boldsymbol{u}=(-\pi\sin(\pi(x-0.5))\cos(\pi(y-0.5)),\ -\pi\cos(\pi(x-0.5))\sin(\pi(y-0.5)))^T.$$

The remaining model parameters are chosen as

$$\mu(c)=\kappa(x,y)=1,\qquad \phi(x,y)=0.1,$$

$$\boldsymbol{D}(\boldsymbol{u})=\begin{pmatrix}1 & 0\\ 0 & 1\end{pmatrix}.$$

In the simulation, the time step is selected as $\Delta t=0.1\min\{\Delta x,\Delta y\}$ and the final time is set to $T=0.01$. The velocity field together with the initial concentration distribution are illustrated in Figure 1. Figure 2 presents the evolution of the numerical concentration at four representative times, namely $\frac{T}{32}$, $\frac{T}{8}$, $\frac{T}{4}$, and T.

From Figure 2, one can observe a gradual reduction of the total concentration mass over time, which reflects the continuous extraction of the fluid mixture through the production well. The computed results demonstrate that the proposed bound-preserving DG method is able to capture the transport dynamics of incompressible miscible displacement accurately while maintaining stable and physically meaningful solutions.

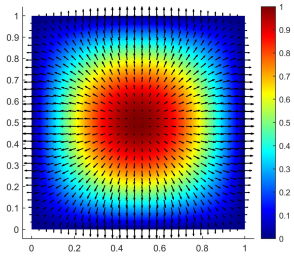

Figure 1. Example 5.3: Velocity Field and Initial Concentration.

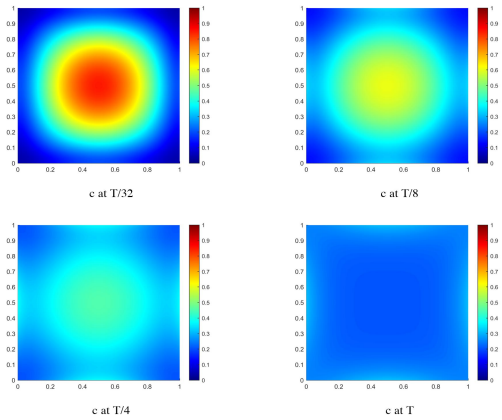

Figure 2. Example 5.3: Evolution of the Bound-Preserving Concentration.

5.3. Source-Free Transport and Mass Conservation

The final test isolates the discrete conservation property. Since q=0, the right-hand side of (58) vanishes and the total porosity-weighted concentration should remain constant. The initial data contain a discontinuity, so a high-order approximation may activate the corrector even though the global mass is fixed.

Example 5.4 (Translation and mass conservation). The initial condition in Example 5.3 is modified as follows:

$$c(x,y,0)=\begin{cases}0.001, & (x-0.5)^2+(y-0.5)^2 \\ & <0.09, \\ 0, & \text{otherwise.}\end{cases}$$

The velocity field is taken as a constant vector $\boldsymbol{u}$=(0.1, 0.4).

The test uses $\Omega=[0,1]^2$ with periodic transport boundaries and retains ϕ=0.1 and $\boldsymbol{D}=\boldsymbol{I}$, and set $\Delta t=0.1\min\{\Delta x,\Delta y\}$ and T=0.01. Consequently, the source term satisfies q=0, indicating that no injection or production wells are present in the computational domain.

The velocity field and the initial concentration distribution are shown in Figure 3. The evolution of the numerical concentration at times $\frac{T}{4}$, $\frac{T}{2}$, $\frac{3T}{4}$, and T is presented in Figure 4. It can be observed that the concentration profile is transported along the direction of the prescribed velocity field, which is consistent with the expected physical behavior of the flow.

For this problem, the total mass of ϕc should remain constant during the time evolution. The numerical results displayed in Figure 5 confirm that the mass is well preserved throughout the simulation. These results demonstrate that the proposed bound-preserving method accurately captures the transport process while maintaining the conservation of mass.

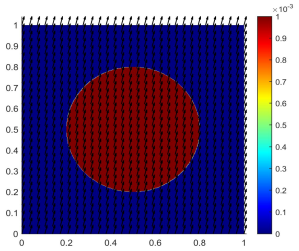

Figure 3. Example 5.4: Velocity Field and Initial Concentration Distribution.

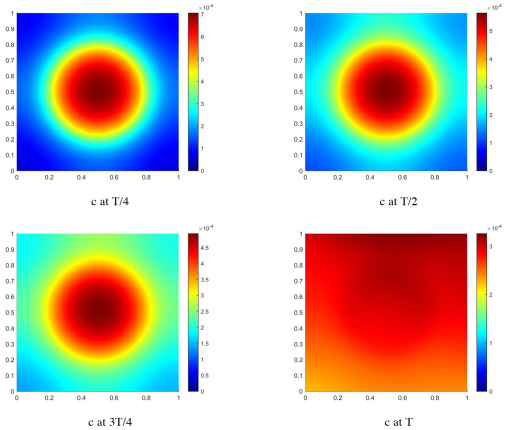

Figure 4. Example 5.4: Translated Concentration at Four Output Times.

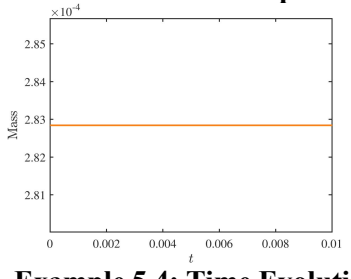

Figure 5. Example 5.4: Time Evolution of the Total Mass of ϕc.

5.4. Field-Oriented Heterogeneous Applications

The last two examples move beyond manufactured coefficients and prescribed velocities. In each case the Darcy pressure is computed from the heterogeneous permeability and a balanced injection–production pair, after which the transport equation is advanced with the same conservative predictor–corrector structure. The nondimensional coordinate domain is $[0,1]^2$; the two domains may be read as a 1 km×1 km reservoir and a 2 km×1 km aquifer, respectively. Time is reported in pore volumes injected,

$$\mathrm{PVI}=\frac{Qt}{\int_\Omega \phi \ \mathrm{d}\boldsymbol{x}}, \tag{65}$$

where Q is the total injection rate. Localized wells are represented by Gaussian profiles of width σ and are normalized so that their integrals are Q and $-Q$. No-flow conditions are imposed on the outer boundary.

These application tests use an 80×80 Cartesian mesh, the piecewise-constant member of W_h, the upwind normal flux, and BDF1. This choice is stated explicitly because the objective is robustness with strong coefficient contrasts rather than a further order test. For P^0 elements the DG balance is algebraically equivalent to the cell-centred conservative balance. The pressure equation is solved with harmonic face permeability, and the scalar mass corrector is retained after every transport step. This implementation therefore preserves the same well balance as (58).

Example 5.5 (Heterogeneous five-spot displacement). The porosity is $\phi=0.20$, the injection and production wells are centred at $(0.08,0.08)$ and $(0.92,0.92)$, and $Q=0.20$. The injected concentration is $\tilde{c}=1$, the initial resident concentration is zero, and $\boldsymbol{D}=2\times10^{-5}\boldsymbol{I}$. With normalized coordinates, the permeability field is

$$\begin{aligned}\log\kappa(x,y)&=1.15\sin(2\pi x)\cos(2\pi y)\\&+0.65\sin(6\pi x+1.1)\sin(4\pi y)\\&+1.15e^{-\left(\frac{y-0.15-0.72x}{0.075}\right)^2}.\end{aligned} \tag{66}$$

The well width is $\sigma=0.028$, and the computation is continued to one PVI.

The permeability varies from 0.2233 to 11.9074. The high-permeability diagonal band in Figure 6 bends the displacement front toward the producer and produces a markedly nonuniform sweep. A production concentration of 0.05 is first reached at 0.396 PVI; by one PVI the production concentration is 0.6649. The final concentration lies in $[3.23\times10^{-10},1]$, and the maximum absolute residual in the accumulated injection–production mass balance is 1.98×10^{-14}. Hence the observed early breakthrough is a permeability-channeling effect rather than a loss of conservation.

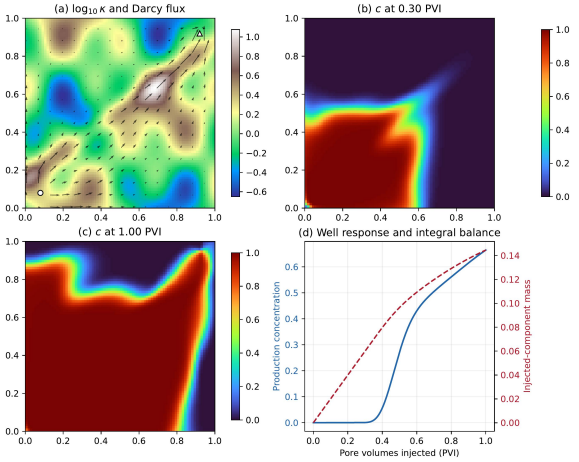

Figure 6. Example 5.5: Heterogeneous Five-Spot Permeability, Concentration Snapshots, Production Response, and Mass Balance.

Example 5.6 (Pump-and-treat remediation in a channelized aquifer). Clean water is injected at $(0.05,0.80)$ and groundwater is extracted at $(0.95,0.25)$, with $Q=0.18$, $\sigma=0.030$, and $\phi=0.25$. The initial contaminant plume and dispersion tensor are

$$c_0(x,y)=0.85\exp\left[-\frac{(x-0.28)^2}{0.012}-\frac{(y-0.72)^2}{0.018}\right], \tag{67}$$
$$\boldsymbol{D}=1.5\times10^{-5}\boldsymbol{I}.$$

The injected water is clean, so $\tilde{c}=0$. The aquifer contains two conductive pathways and a vertical barrier:

$$\begin{aligned}\kappa(x,y)=b(x,y)(&0.16\\&+6\exp\left[-\left(\frac{y-0.20-0.42x}{0.055}\right)^2\right]\\&+2.8\exp\left[-\left(\frac{y-0.76}{0.070}\right)^2\right]).\end{aligned} \tag{68}$$

Let $\mathscr{B}$ denote the barrier region defined by $|x-0.58|<0.035$ and $|y-0.32|>0.10$. Then

$$b(x,y)=\begin{cases}0.06, & (x,y)\in\mathscr{B},\\ 1, & \text{otherwise.}\end{cases} \tag{69}$$

The simulation is run to 1.5 PVI.

The permeability contrast is approximately 646:1. As shown in Figure 7, the upper channel first carries part of the plume toward the barrier, while the gap and the oblique lower channel redirect contaminated water to the extraction well. The extracted concentration exceeds 0.05 at 0.349 PVI and reaches its maximum value 0.1483 at 0.453 PVI. It then decays to 1.46×10^{-3} at 1.5 PVI. At that time 96.42% of the initial contaminant mass has been removed, the remaining

concentration belongs to [0,0.04162] , and the maximum absolute mass-balance residual is 1.65×10^{-15} . The tail of the removal curve is consistent with slow release from the low-velocity regions separated by the barrier.

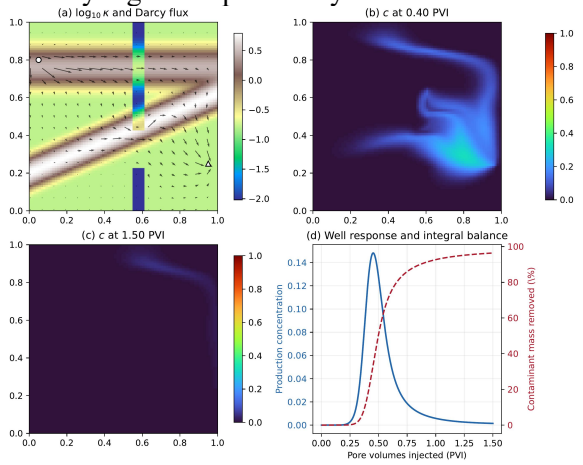

Figure 7. Example 5.6: Pump-and-Treat Remediation, Flow Pathways, Concentration Snapshots, and Contaminant Removal.

Table 3 collects the principal diagnostics. In both cases the provisional P^0 update was already admissible, so the corrector changed it only at roundoff level. This is consistent with the monotonicity of the implicit upwind P^0 predictor; the high-order tests in Examples 5.1–5.4 remain the cases in which the active-set correction is essential.

Table 3. Summary of the Two Heterogeneous Application Tests.

Diagnostic	Five-spot	Remediation
Minimum permeability	0.2233	0.0096
Maximum permeability	11.9074	6.2040
Characteristic response	0.396 PVI (5% breakthrough)	96.42% removed
Final range of c	$[3.23\times10^{-10}, 1]$	[0, 0.04162]
Mass residual	1.98×10^{-14}	1.65×10^{-15}

6. Conclusion

A high-order implicit bound-preserving DG method has been developed for incompressible miscible displacement. The spatial discretization combines alternating Darcy fluxes, upwind convection, and an interior-penalty treatment of dispersion. Consistent fluxes retain the two-component identity and give a local and global discrete mass balance. The temporal discretization is based on BDF formulas and is separated into an implicit DG prediction and a Lagrange multiplier correction.

The interval constraint is expressed through $g(c)=c(1-c)$ and the associated KKT conditions. Once the scalar mass multiplier is fixed, the corrector is solved pointwise by a three-branch formula. The scalar multiplier is determined from a continuous monotone mass equation and can be computed by a safeguarded secant iteration. The method therefore enforces $0\le c_h\le1$ without adding a global constrained system to the pressure–transport solve. It also preserves the BDF discretization of the physical well balance, rather than imposing constant mass when sources are present.

The manufactured-solution results show third-order convergence for the corrected and uncorrected approximations. In the uncorrected computations, small undershoots and overshoots occur on several meshes; the Lagrange multiplier step removes them without changing the measured order. The controlled flow examples illustrate the transport of bounded concentration profiles and confirm mass conservation for the source-free problem. The two heterogeneous applications additionally show preferential breakthrough in a five-spot pattern and effective plume capture in a pump-and-treat configuration. Their accumulated injection–production balances close to near machine precision, even in the presence of permeability contrasts exceeding two orders of magnitude.

Further work includes a complete error analysis for the fully coupled nonlinear Darcy–transport system, extensions to nonmatching and adaptive meshes, and the design of efficient solvers for strongly heterogeneous permeability and velocity-dependent dispersion. The multiplier formulation is also suitable for multicomponent models with more than two concentrations, where the admissible set becomes a simplex rather than an interval.

References

[1] M.F. Wheeler, B.L. Darlow. Interior penalty Galerkin procedures for miscible displacement problems in porous media. In: Computational Methods in Nonlinear Mechanics, North-Holland, Amsterdam, 1980, pp. 458–506.

[2] B. Rivière. Discontinuous Galerkin Finite Element Methods for Solving the Miscible Displacement Problem in Porous Media. PhD thesis, The University of Texas at Austin, Austin, TX, 2000.

[3] S. Sun, B. Rivière, M.F. Wheeler. A combined mixed finite element and discontinuous Galerkin method for miscible displacement problem in porous media In: Tony Chan, et al. (Eds.), Recent Progress in Computational and Applied PDEs, Kluwer Academic Publishers, Plenum Press, Dordrecht, New York, 2002, pp. 323–351.

[4] S. Sun, M.F. Wheeler. Discontinuous Galerkin methods for coupled flow and reactive transport problems. Applied Numerical Mathematics, 2005, 52: 273–298.

[5] H. Guo, Q. Zhang, Y. Yang. A combined mixed finite element method and local discontinuous Galerkin method for miscible displacement problem in porous media. Science China Mathematics, 2014, 57: 2301–2320.

[6] S. Bartels, M. Jensen, R. Müller. Discontinuous Galerkin finite element convergence for incompressible miscible displacement problems of low regularity. SIAM Journal on Numerical Analysis, 2009, 47: 3720–3743.

[7] B. Cockburn, C.-W. Shu. The local Discontinuous Galerkin method for time-dependent convection-diffusion systems. SIAM Journal on Numerical Analysis, 1998, 35(6): 2440–2463.

[8] B. Rivière. Discontinuous Galerkin methods for solving elliptic and parabolic equations: theory and implementation. SIAM, 2008.

[9] X. Guo, H. Guo, L. Tian, Y. Yang. High-order bound-preserving local discontinuous Galerkin methods for incompressible and immiscible two-phase flows in porous media. Journal of Scientific Computing, 2024, 99: 71.

[10] K. L. A. Kirk, B. Riviere. A combined mixed hybrid and hybridizable discontinuous Galerkin method for Darcy flow and transport. Journal of Scientific Computing, 2024, 100(2): 57.

[11] Y. Kang, T. Xiong, Y. Yang. Oscillation-free implicit pressure explicit concentration discontinuous Galerkin methods for compressible miscible displacements with applications in viscous fingering. Journal of Computational Physics, 2024, 516: 113348.

[12] M. S. Fabien. A cell centered Galerkin method for miscible displacement in heterogeneous porous media. Computer Methods in Applied Mechanics and Engineering, 2026, 450: 118608.

[13] X. Zhang, C.-W. Shu. On maximum-principle-satisfying high order schemes for scalar conservation laws. Journal of Computational Physics, 2010, 229: 3091–3120.

[14] X. Zhang, C.-W. Shu. On positivity preserving high order discontinuous Galerkin schemes for compressible Euler equations on rectangular meshes. Journal of Computational Physics, 2010, 229: 8918–8934.

[15] X. Zhang, C.-W. Shu. Positivity-preserving high order discontinuous Galerkin schemes for compressible Euler equations with source terms. Journal of Computational Physics, 2011, 230: 1238-1248.

[16] Y. Zhang, X. Zhang, C.-W. Shu. Maximum-principle-satisfying second order discontinuous Galerkin schemes for convection-diffusion equations on triangular meshes. Journal of Computational Physics, 2013, 234: 295–316.

[17] H. Guo, Y. Yang. Bound-preserving discontinuous Galerkin method for compressible miscible displacement in porous media. SIAM Journal on Scientific Computing, 2017, 39: A1969–A1990.

[18] Q. Cheng, J. Shen. A new Lagrange multiplier approach for constructing structure preserving schemes, I. Positivity preserving. Computer Methods in Applied Mechanics and Engineering, 2022, 391: 114585.

[19] Q. Cheng, J. Shen. A new Lagrange multiplier approach for constructing structure preserving schemes, II. Bound preserving. SIAM Journal on Numerical Analysis, 2022, 60(3): 970-998.

